Materials LAB

PERSPECTIVE

*Materials Lab* 2025, 4, 250002

# Electron microscopy measurements of electron orbitals

Guodong Zhu[1], Qinghua Zhang[2] and Lin Gu[1]*

**Quantitative characterization and real-space mapping of the electron orbital are highly desirable as it's a basic order parameter linking microscopic electronic structure and macroscopic properties in material science. Here we briefly review the recent progress in the measurements of orbital populations via electron microscopic methods, including quantitative convergent-beam electron diffraction (QCBED), electron energy-loss spectroscopy (EELS) and others. Combing with the rapid development of four-dimensional scanning transmission electron microscopy (4D-STEM), we propose the future potential directions and discuss possible solutions towards real-space orbital mapping at atomic scale.**

The origin of functionality for functional materials is closely related to local symmetry breaking[1], which is described in four degrees of freedom: lattice, charge, orbital, and spin. Among them, the orbital is an important manifestation of the local electronic structure. As a microscopic basis, its quantitative characterization is beneficial to the better understanding of macroscopic phenomena and functional properties[2]. Although the real-space resolution of electron microscopy has reached sub-angstrom level; a recent resolution record of 14 picometers has been demonstrated by electron ptychography[3–4], how to characterize the local electronic structure in real space is still challenging, especially at atomic scale.

From the perspective of quantum mechanics, it is generally believed that orbitals cannot be directly "seen" in real space[5]. Since Zuo et al. reported the direct observation of *d*-orbital holes and Cu-Cu bonding in $Cu_2O$ more than two decades ago[6], there have been many debates around whether orbitals can be claimed to be experimentally visible[7–10]. It has been argued that the so-called orbitals are actually just three-dimensional charge density maps that do not directly reflect the occupation states of different orbitals. Although orbital observation has been mentioned many times[11–12], it is often analyzed only for a specific problem of particular materials. We believe that the exploration and discussion of orbital measurements is worthwhile, at the very least, highly beneficial in shedding light on electronic states with orbital degrees of freedom and their effect on physical properties[13–15]. In this paper, we review the recent progress on the orbital observation with several electron microscopic methods including quantitative convergent-beam electron diffraction (QCBED), electron energy-loss spectroscopy (EELS) and others. We also propose some intuitional thinking for real-space local orbital observation in terms of four-dimensional scanning transmission electron microscopy in the perspective part.

## QCBED

The first observation of orbitals was reported in $Cu_2O$ through the electron density fitted by the multipole model[6] in 1999, based on structure factors fitted by QCBED and X-ray diffraction. This method of QCBED fitting had also been applied to image charge density distributions of $Ni_3Al$[16]. A systematic review on the fitting of structure factors has also been carried out[17–18]; Zuo et al. summarized the experimental measurements of the charge density distribution in solids and the corresponding chemical bonding interpretations[19] in 2004. On the basis of QCBED, Wu et al. have also developed a novel electron-diffraction technique in 1999, called parallel recording of dark-field images (PARODI), which focused the probe above or below the sample[20–22]. This method was applied beyond the traditional QCBED limitations for small crystals to the large cell unit structure of high-temperature superconductors, experimentally revealing small changes in the valence electron distribution in $YBa_2Cu_3O_7$ and $Bi_2Sr_2CaCu_2O_{8+\delta}$ [21]. In addition, there have also been many studies that have utilized QCBED to map charge density or deformation charge density and relate it to valence electrons or bonding information, including first-principle aided calculations and validation[23–29].

It should be noted that the multipole model used to fit the electron density is the key to differentiate orbitals in $Cu_2O$ from other QCBED studies for mapping charge density. This model was first proposed as an X-ray crystallographic method for analyzing electron density[30], which includes the non-spherical part to describe charge density. For *d*-orbital electrons, it is possible to correlate the multipole parameters with the *d*-orbital occupation based on the equivalence of the valence electron part of the multipole function for the charge density with the atomic orbital description[31].

[1] *Beijing National Center for Electron Microscopy and Laboratory of Advanced Materials, School of Materials Science and Engineering, Tsinghua University, Beijing 100084, China*

[2] *Beijing National Laboratory for Condensed Matter Physics, Collaborative Innovation Center of Quantum Matter, Institute of Physics, Chinese Academy of Sciences, Beijing 100190, China*

* Corresponding author, E-mail: lingu@mail.tsinghua.edu.cn

Received 21 January 2025; Accepted 4 March 2025; Published online 5 March 2025

DOI: 10.54227/mlab.20250002

In 2022, Shang et al. combined QCBED with the multipole model again to study the evolution of valence electrons of Co and O atoms in $Li_{1-x}CoO_2$ with different charging states during the charging process[32]. They also established the relationship between the *d*-orbital populations and the multipole density function by measuring the distribution of the non-spherical electron density and explained the correlation between the crystal structure and the electronic structure from the orbital point of view. As shown in Fig. 1[32], the shapes of $e_g$ and $t_{2g}$ orbitals of Co and *2p* orbitals of O in the $CoO_6$ octahedral crystal field can be clearly observed in the initial $LiCoO_2$ deformation charge density map. In this map, the differences in the regional colors represent the differences in the electron aggregation states, thus indicating that the *3d* electrons preferentially occupy the $t_{2g}$ orbitals of Co atoms over the $e_g$ orbitals in the $CoO_6$ octahedron. Comparison of the different charging states shows the difference in the number of occupied electrons in the $t_{2g}$ and $e_g$ orbitals and the change in the electron density near the O atom, which suggests that charge transfer from the ligand to the metal atom occurs in $Li_{1-x}CoO_2$ as the concentration of Li vacancies increases and electrons are transferred from the O *2p* orbitals to the Co $e_g$ orbitals.

After that, Tang et al. obtained structure factors with the combination of QCBED and synchrotron powder X-ray diffraction (SPXRD) and reconstructed the 3D charge density distribution of ScS based on multipole model fitting in 2023[33]. With the deformation charge density map of the (100) surface of ScS and the fit multipole parameters, they investigated the electronic configuration of $Sc^{2+}$ in ScS, proving that its remaining outer layer was *4s* instead of *3d* electrons. In addition to SPXRD assisted to obtain high-order structure factors, the charge density distribution and multipole fitting parameters can also be obtained with the high-order structure factors calculated from density functional theory (DFT)[29] and the low-order structure factors fit from QCBED experiments. Based on this method, the *3d*-orbital electron distribution of Mn in $LiMn_2O_4$ and $Li_{0.5}Mn_2O_4$ was measured by Shang et al. in 2024[34]. The diagram of experiments and the strategy is shown in Fig. 2. The $d_{z^2}$ and $d_{x^2-y^2}$ orbital electron occupations of Mn were found to be essentially the same, indicating the degeneracy of the $e_g$ orbitals. Taking the symmetry of the ligand oxygen atoms in the $MnO_6$ octahedron even further, an orbital strategy is proposed to directly modulate the local coordination configuration of the Jahn-Teller distortion.

## EELS

The electron energy-loss spectroscopy is based on inelastic scattering from the interaction of the incident electron beam and the sample[35], whereas the latest STEM-EELS allows for the simultaneous acquisition of a dataset by the EELS spectrometer after the STEM scanning of a region, thus obtaining a three-dimensional informative dataset that contains both position and energy[36].The STEM-EELS can provide information on bonding between different atoms, valence states and fine electronic structures in addition to information on elemental composition. Löffler et al. first demonstrated it on theoretical grounds that real-space mapping of transitions between orbitals on the Ångström scale should indeed be possible by energy-filtered TEM (EFTEM) in 2013 and 2016[37–38]. They then proposed to implement real-space mapping of electronic orbitals and reveal information on individual bonds between atoms in Rutile with STEM-EELS in 2017[39]. Fig. 3[39] shows that energy windows of $e_g$ and $t_{2g}$ were fit in Ti $L_{2,3}$ edge. Experimental energy-filtered map for the Ti *L* ionization edge for final states with $e_g$ character matched the simulated image very well and showed a distinct asymmetry towards the nearest O atoms, which could be attributed to the orbitals. The orbital characteristics of anions in coordination environments, such as O in the $Cu_2O$ plane of high-temperature cuprate superconductors[40–41], have also been previously investigated using energy-loss near-edge structure (ELNES) of EELS in 1990s, but did not involve orbital mapping. Similarly,

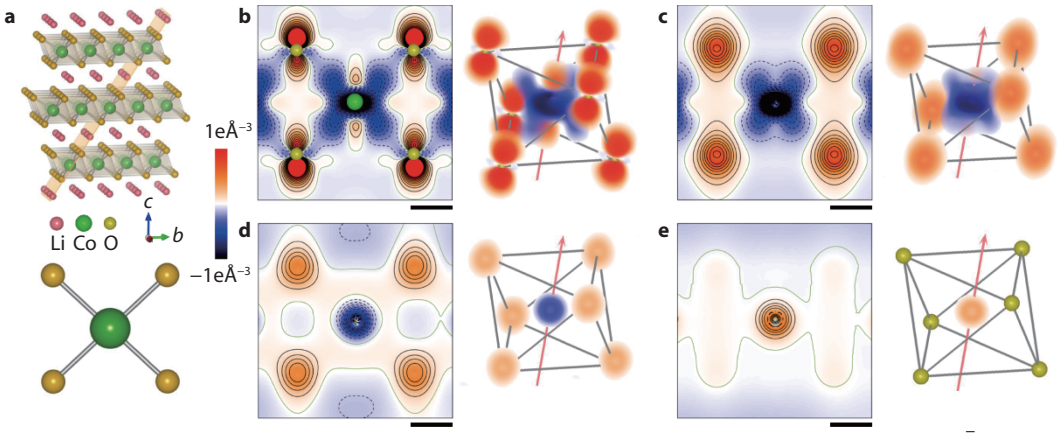


**Fig. 1** Electron density evolution of the Co–O and O–O interactions. **a** Structural model of $LiCoO_2$ with the indexed $(\bar{1}01\ 4)$ plane near the [100] direction (top). $CoO_4$ $(\bar{1}01\ 4)$ plane of the $CoO_6$ octahedra (bottom). **b**–**e** Static deformation density maps of the $(\bar{1}01\ 4)$ $CoO_4$ plane and corresponding three-dimensional (3D) views of **b** $LiCoO_2$, **c** $Li_{0.6}CoO_2$, **d** $Li_{0.4}CoO_2$, and **e** $Li_{0.3}CoO_2$. The electron density is present in different colors with the color scale shown on the left. The red color region means the electron density accumulation, and the blue color region represents the electron density depletion. All of the maps use a contour interval of 0.1 *e* Å$^{-3}$, with positive, negative, and zero contours drawn as solid black, dashed black, and solid olive-green lines, respectively. The inclined arrows show the [001] direction, and all of the 3D views use the same color scheme. All scale bars indicate 1 Å[32]. Copyright 2022, Springer Nature.

DOI: 10.54227/mlab.20250002

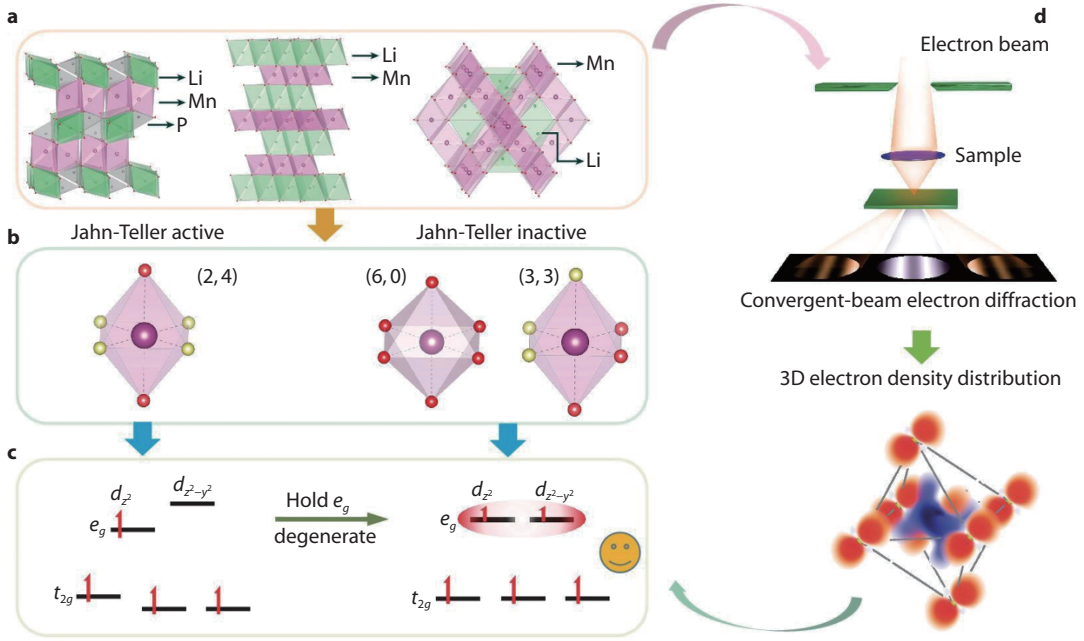


**Fig. 2** Orbital strategy to control the Jahn–Teller effects (JTE). **a** Three common structure models (olivine, layered, spinel) of cathode materials for rechargeable Li-ion battery. **b** $MnO_6$ octahedra with different symmetries. Ligands with the same color are identical and vice versa. The left octahedron is JT active, while the right two octahedra are JT inactive. **c** The orbital strategy to maintain the degeneracy of $e_g$ levels to suppress the JTE. **d** By combining convergent-beam electron diffraction and density functional theory (DFT) calculations, *d*-orbital occupancy can be quantified, and therefore the JTE can be detected [34]. Copyright 2024, Oxford University Press.

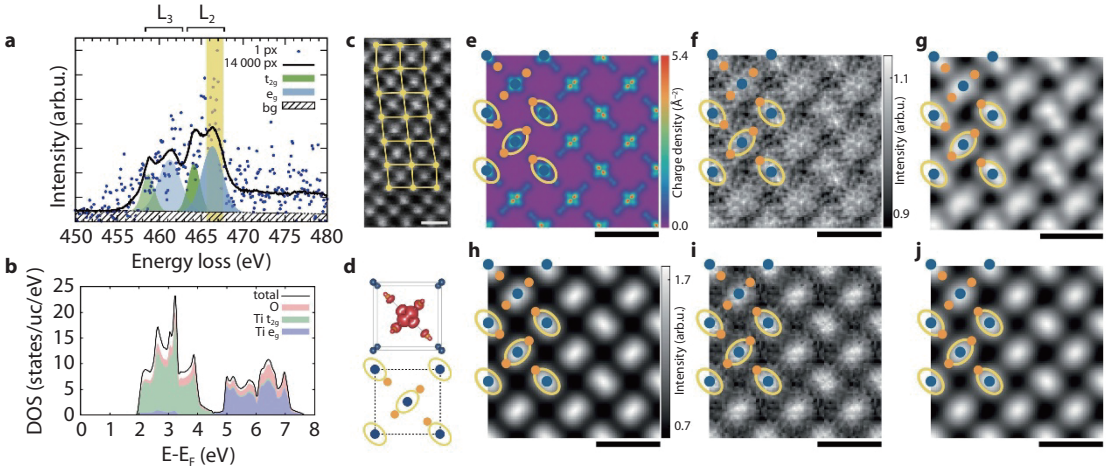


**Fig. 3** Real-space mapping of electronic orbitals in Rutile with STEM-EELS. **a** Ti $L_{2,3}$ edge extracted from a single pixel (dots), and averaged over all 14000 pixels (line) of the data set. The energy window used for the energy-filtered $e_g$ maps is highlighted in yellow. Gaussian least squares fits representing the individual shapes of the $e_g$ and $t_{2g}$ contributions are depicted in blue and green. **b** Projected DOS above the Fermi energy $E_F$ calculated by WIEN2k. **c** Dark field image acquired simultaneously with the spectrum image dataset. **d** Unit cell along the [0 0 1] direction used in the experiment with the summed three-dimensional charge density of the $e_g$ Wannier functions. Also shown are the projected positions of Ti (blue) and O (orange) atoms as well as yellow ellipses indicating the nearest O neighbours of each Ti (due to the projection, only two of the four nearest neighbours are visible). **e** Charge density for the unoccupied $e_g$ orbitals projected along the [0 0 1] crystallographic axis as calculated by WIEN2k. **f** Experimental energy-filtered map for the Ti *L* ionization edge for final states with $e_g$ character after unit-cell averaging. **g** Same as **f**, but after Gaussian smoothing. **h** Simulated energy-filtered map using the multislice algorithm and the mixed dynamic form factor approach after Gaussian blurring. **i** Same as **h** with added noise to better mimic the experimental conditions. **j** Same as **i** after Gaussian smoothing. All maps are replicated in a 3 × 3 raster for better visibility. Overlays show the projected positions of Ti and O atoms as well as yellow ellipses indicating the nearest O neighbours of each Ti. All scale bars indicate 5 Å[39]. Copyright 2017, Elsevier.

the relation between local structural distortions in the $PbTiO_3/SrTiO_3$ superlattice interface and the splitting of the *3d* orbitals of Ti atoms in crystal field has been studied by Torres-Pardo et al. by combining STEM and EELS without direct mapping of orbitals in 2011[42].

Xu et al.'s study of quantum-order parameters in bismuth-doped iron garnet not only analyzed the splitting of Fe *3d* orbital state of in different crystal fields using energy shifts and

DOI: 10.54227/mlab.20250002

fine features in the $L_{2,3}$ edges of EELS, but also synergistically measured the spin configuration with electron magnetic circular dichroism (EMCD), thus revealing the coupling effects between multiple quantum-order parameters in 2021[43]. Meanwhile, Iwashimizu et al. combined the STEM-EELS with the multiple frame acquisition approach to improve the signal-to-noise ratio (SNR) for spectra in spectrum imaging data and achieved the visualization of 2*p* electron orbitals of oxygen in $SrTiO_3$ in real space, which agreed well with the simulated charge density distribution of DFT for the energy selected unoccupied O 2*p* orbitals[44]. Bugnet et al also combined the STEM-EELS with inelastic channeling calculations to present real-space maps of $\pi^*$ and $\sigma^*$ states in epitaxial graphene multilayers and highlight the direct mapping of the $\pi^*$ state distribution at atomic resolution by the interpretation of the spatial distribution of orbital signals in 2022[45]. Moreover, they demonstrated the decisive effect of the specimen thickness on the orbital mapping capabilities in graphene with calculations. Recently, Ederer et al. investigated representative examples of a transition metal oxide and an interface between two different materials to optimize experimental parameters for orbital mapping with EELS in 2024, including sample thickness, acceleration voltage and electron dose for probe as well as parallel illumination[46]. They employed an image difference metric based on the scale invariant feature transform (SIFT) algorithm to evaluate the effects of different parameter settings by simulations, which involved the density functional theory and electron channeling simulations. Fig. 4[46] shows the orbital mapping by O K-edge in a heterostructure consisting of the two perovskites $SrTiO_3$ (STO) and $LaMnO_3$ (LMO) based on simulations. The *p*-like orbitals oriented perpendicular to each other were clearly observed in the STO region, while those were blurry and less distinct in the LMO region due to the rotation of the $MnO_6$ octahedra. The results also demonstrated the effects of different parameters on the orbital map quality.

## Other methods

### EDX

Energy-dispersive x-ray (EDX) works with analyzing energy in the form of x-ray produced by the decay of excited core electrons[36]. Atomic-resolution chemical mapping by EDX in STEM was initially demonstrated by D'Alfonso et al. in 2010[47]. They also highlighted the combination of simultaneous STEM EELS, HAADF and EDX, which could be powerful for analyzing structural chemical and functional information at the atomic resolution. Jeong et al. probed core-level electron orbitals of Sr and Ti in real space by recording low-noise EDX spectroscopy maps from a $SrTiO_3$ crystal in 2016[48]. The experiments also measured the electronic excitation impact parameter and the delocalization of an excitation due to Coulombic beam-orbital interaction. The core-level electron orbitals of Sr and Ti, i.e., *1s* and *2p*, were probed from *K* and *L* x rays, which were produced solely by filling empty states. Therefore, each x-ray map, where the effects of source size smearing and beam channeling were removed, could be regarded as spatially resolved measurements of core-electron excitation probability for a specific orbital. The probed core-level electron orbitals smeared due to thermal vibrations of

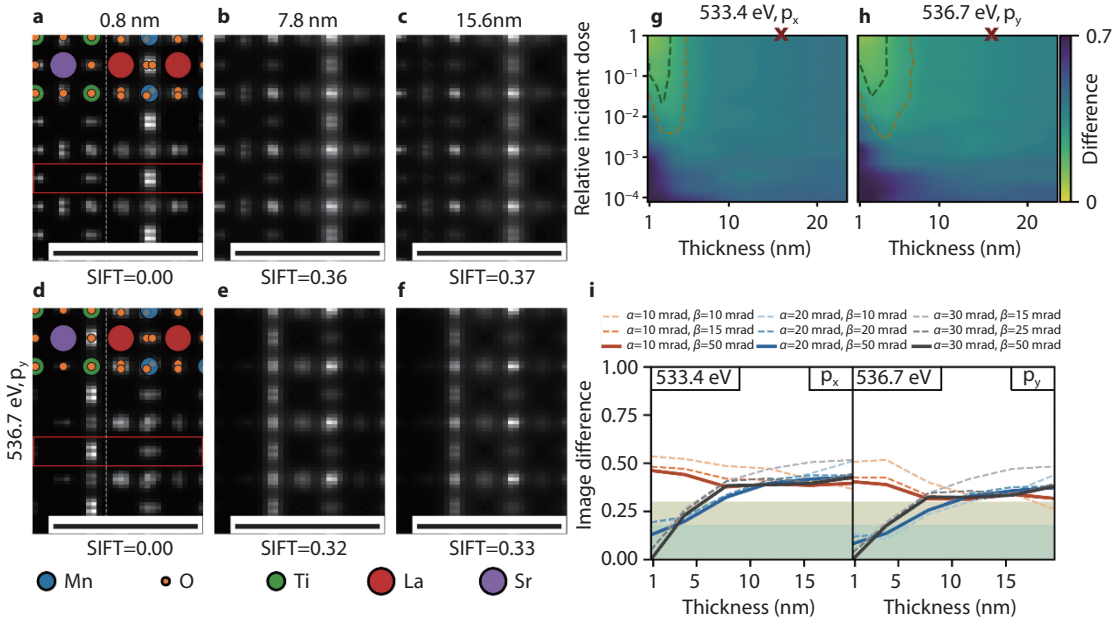


**Fig. 4** Optimizing experimental parameters for orbital mapping in a heterostructure with EELS. **a**-**f** Simulated STEM spectrum images of the interface between STO and LMO in the [100] zone axis for both materials, the indicated sample thickness and energy loss with an infinite electron dose. All scale bars indicate 1 nm. **g**-**h** Image difference maps of the STO-LMO spectrum images for the indicated energy losses. The incident dose is measured relative to the image dose of $10^6$ $e^-/nm^2$ for the image of a 15.6 nm thick sample, marked by the red x. The reference image in all cases is calculated with infinite electron dose. The dark green and olive contour lines indicate an image difference of 0.18 and 0.3, respectively. **i** STO-LMO SIFT image difference as a function of sample thickness for an acceleration voltage of 300 kV and several convergence and collection semi-angles $\alpha$ and $\beta$. All image differences are relative to the orbital map for $\alpha = 30$ mrad and $\beta = 50$ mrad[46]. Copyright 2024, Elsevier.

DOI: 10.54227/mlab.20250002

the atoms and excitation broadening are shown in Fig. 5[48].

### STM

Scanning tunneling microscopy (STM) is based on the vacuum tunneling of electrons between a sharp tip and a sample, which can be used to measure surface chemistry and electronic structure[36]. STM can not only move and position single atoms and molecules, but also be applied to manipulate the bonding of molecules[49] and directly image the orbital hybridization upon bond formation[50]. Moreover, Gross et al. have reported high-resolution molecular orbital imaging using a *p*-wave STM tip in 2011[51]. Their studies indicated for naphthalocyanine molecules on the same substrate, the closely spaced nodal planes were difficult to resolve with an *s*-wave tip but could be effectively visualized with a *p*-wave tip, enhancing contrast and revealing additional information of the orbital structure, including in the central region, as shown in Fig. 6[51]. These findings underscored the significant contribution of *p*-wave tip effects in STM orbital imaging due to tunneling through the $\pi$ orbitals of the CO tip.

Surface-assisted orbital order on a cobalt-terminated surface of the heavy fermion compound $CeCoIn_5$ was also visualized by STM on the atomic scale in 2017[52]. First-principles calculations revealed that the staggered $d_{xz}$-$d_{yz}$ orbital order triggered by enhanced on-site Coulomb interactions resulted in dumbbell-shaped cobalt atoms alternating along the [100] and [010] directions. In addition, sublattice-resolved imaging of charge transfer energies by STM has recently been introduced to $CuO_2$ studies and discovered the orbital ordering in $Bi_2Sr_2CaCu_2O_{8+x}$ in 2024[53]. The spectroscopic imaging STM visualized charge transfer energy variations, which revealed the internal electronic structure of orbitally ordered $CuO_2$. As shown in Fig. 7, energy splitting of $O_x$ and $O_y$ orbitals on the 50 meV scale broke the $C_4$ rotation symmetry about every Cu site. These results suggested that the $2p^6$ O orbital at $O_x$ exhibited an energy separation from the upper Cu band that is distinct from that at $O_y$, namely, the existence of intra-unit-cell orbital order.

### X-ray

For high resolution in X-rays, Hafiz et al. reported the use of inelastic scattering spectroscopy of high-energy X-ray photons to visualize redox orbitals in advanced lithium-ion battery materials in 2017, while the mapping of orbitals was in momentum space[54]. In contrast, Yavaş et al. imaged the active orbital in real space with inelastic X-ray scattering in 2019[55]. Moreover, Kitou et al. proposed the core differential Fourier synthesis (CDFS) analysis of high-energy x-ray diffraction data for visualization of *d*-orbital electrons in 2020[56–57], which showed promise in terms of real-space resolution. Noted that the multipole model that can fit charge density has been widely used in X-ray diffraction, such as charge density mapping of organic and inorganic crystals[58–61], however the X-ray diffraction lacked the real-space resolution available in microscopy.

## Discussion and perspective

Each of the techniques introduced above has its unique strengths and limitations when it comes to the measurement and mapping of electron orbitals. QCBED is particularly suitable for perfect crystals, offering a wealth of information

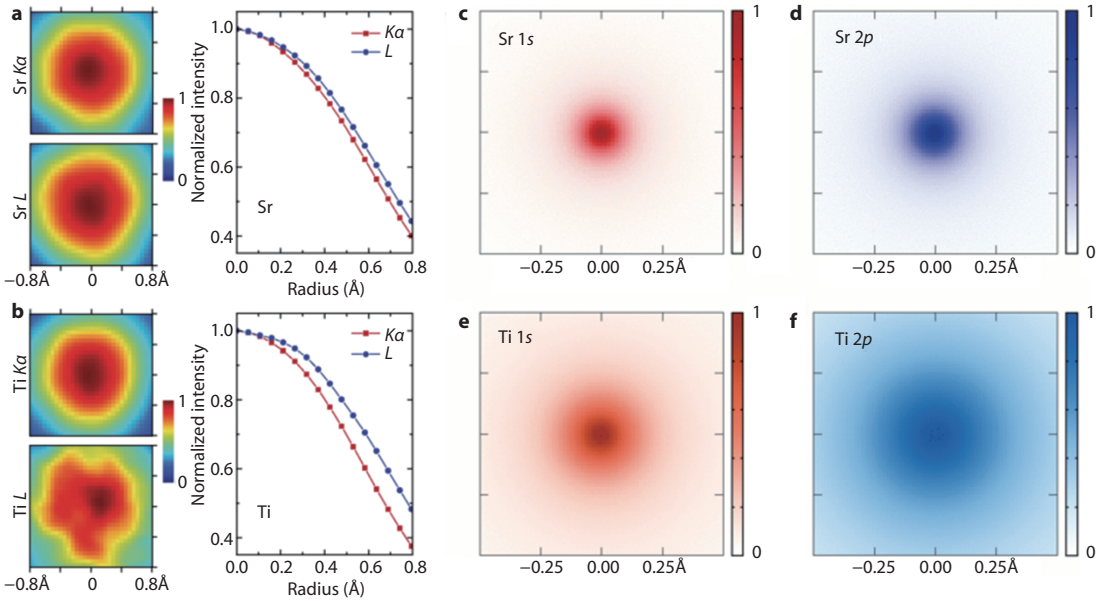


**Fig. 5** Probing core-electron orbitals of Sr and Ti atoms in $SrTiO_3$ with STEM-EDX. **a** Individual Sr *Kα* and *L* EDX maps from the Sr column of STO viewed along the [001] crystallographic direction. **b** Individual Ti *Kα* and *L* EDX maps from the Ti/O column of STO viewed along the same direction. The less circular shape of the Ti *L* map is due to a much lower signal-to-noise ratio in the data, showing that the Ti *L* signal still needs to be improved. For direct comparison, maps are background subtracted and normalized to their central intensity. Azimuthally averaged radial profiles are presented at right for better comparison. These maps constitute the cross-correlated average of data from approximately 450 identical atomic columns and all obtained simultaneously in a single experiment. **c**-**f** Experimentally observed projected excitation potentials for 1*s* and 2*p* orbitals of Sr and Ti, including the effects of atomic thermal vibrations and excitation broadening[48]. Copyright 2016, American Physical Society.

DOI: 10.54227/mlab.20250002

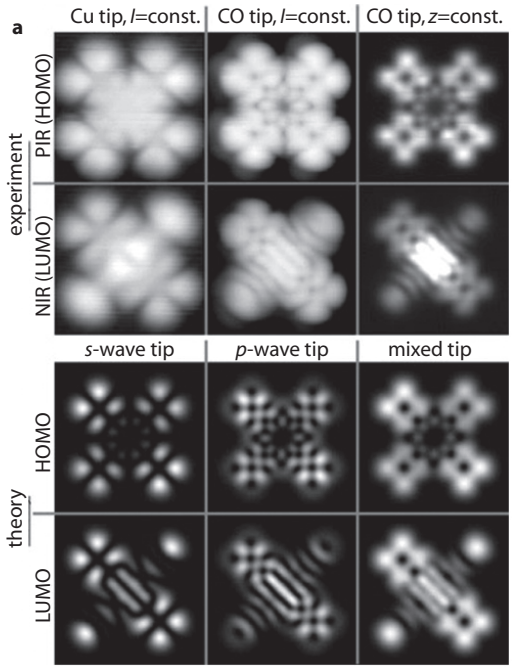


**Fig. 6** High-resolution molecular orbital imaging with STM. **a** Naphthalocyanine on NaCl (2 ML) on Cu (111) measured using a Cu tip, a CO tip in constant-current mode, and a CO tip in constant-height mode. The PIR (1st row) is measured at V=−1.65 V and the NIR (2nd row) at V=0.60 V. **b** Calculated images at $z_0$=5.0 Å of the HOMO (3rd row) and LUMO (4th row) with an s-wave tip, a p-wave tip, and a mixed tip. All images: 27 Å×27 Å[51]. Copyright 2011, American Physical Society.

about the electron density distribution and electron orbitals. However, due to its nature as an average over the reciprocal space, QCBED lacks real-space resolution, making it less appropriate for studying interfaces and defects. EELS provides real-space resolution and is capable of extracting orbital information based on fine features, which is limited to characterizing specific electron states and may not provide a comprehensive view of the entire electron orbital structure. EDX is based on the energy differences to separate electrons from different core levels but has not been applied to the measurement of valence electron orbitals. EDX excels in elemental analysis but falls short in providing detailed orbital information. STM offers high real-space resolution and is excellent for characterizing surface electron states. However, its application is restricted to the surface, and it cannot measure the electron orbitals within the bulk of the materials. X-ray techniques, while less restrictive in terms of sample preparation and minimally destructive, do not possess the real-space resolution capabilities of electron microscopy methods. They are valuable for bulk structural analysis but are not ideal for detailed orbital mapping in real space. In conclusion, the choice of techniques for measuring and mapping electron orbitals depends on the specific needs of experiments, the nature of samples, and the information one aims to extract. Each method has its niche, and a combination of techniques may often be employed to achieve a more complete understanding of the electronic structure.

Based the above overview on electron orbital population measurements and its real-space mapping, we would like to make some outlooks in the context of the recent development of four-dimensional scanning transmission electron microscopy (4D-STEM). 4D-STEM has a unique advantage in terms of real-space imaging resolution, in particular its combination of diffraction with real-space positions, yielding a large amount of information reflecting the properties of the samples[62]. Studies have been realized with the help of 4D-STEM to accurately map the projected charge density of 2D materials[63–64] and heterojunction interfaces[65], valence electron density[66], charge transfer[67], etc. However, none of these studies claimed the experimental electron orbital measurements or mapping. Based on the STEM-EELS methods, Löffler et al. emphasized the possibility of utilizing energy-filtered 4D-STEM with fast, pixelated detectors for mapping inelastic transitions to individual orbitals[68]. By combining the multipole model and 4D-STEM, it should be possible to relate valence electron density with orbital populations.

Notably, Wu et al. have introduced multipolar function formalism to dynamical electron diffraction calculations and simulated CBED patterns of 4D-STEM[69]. They mapped aspherical valence electron distributions from the whole 4D-STEM dataset and demonstrated its sensitivity to charge transfer and aspherical electron orbitals. However, this method is only an attempt in simulations and does not introduce the complex influences that may be present in experiments, nor does it demonstrate the validity of the multipolar function formalism for valence electrons in 4D-STEM experiments. Perhaps simulations starting from multipolar function formalism can be generalized into iterative fits of initial covariates to experimental data to optimize multipolar parameters and account for orbital populations, with similar iterations as implemented in the ptychography[4].

On the other hand, considering the experimental realization conditions, the existing setup and acquisition methods may be improved to increase the signal of valence electrons experimentally, thus creating a solid basis for the real-space sensitivity for orbital electron changes. Artificial intelligence may also give rise to new ways of analyzing electron microscopy data[70–71]. In addition, in-situ experiments are expected to be designed for better separating the contribution of valence electrons and even orbital populations, and provide more reliable correlation between the functional properties and electronic structures of materials.

## ■ ACKNOWLEDGEMENTS

This work was supported by the National Key R&D Program of China (Grant No. 2022YFB2404400, 2024YFA1409500), National Natural Science Foundation of China (Grant No. 52025025, 52250402, 52322212) and the Science Fund for Creative Research Groups of the National Natural Science Foundation of China (Grant No. 52421001).

## ■ CONFLICT OF INTEREST

The authors declare no conflict of interest

## ■ AUTHOR CONTRIBUTIONS

This manuscript was drafted by G. Zhu, Q. Zhang and re-

DOI: 10.54227/mlab.20250002

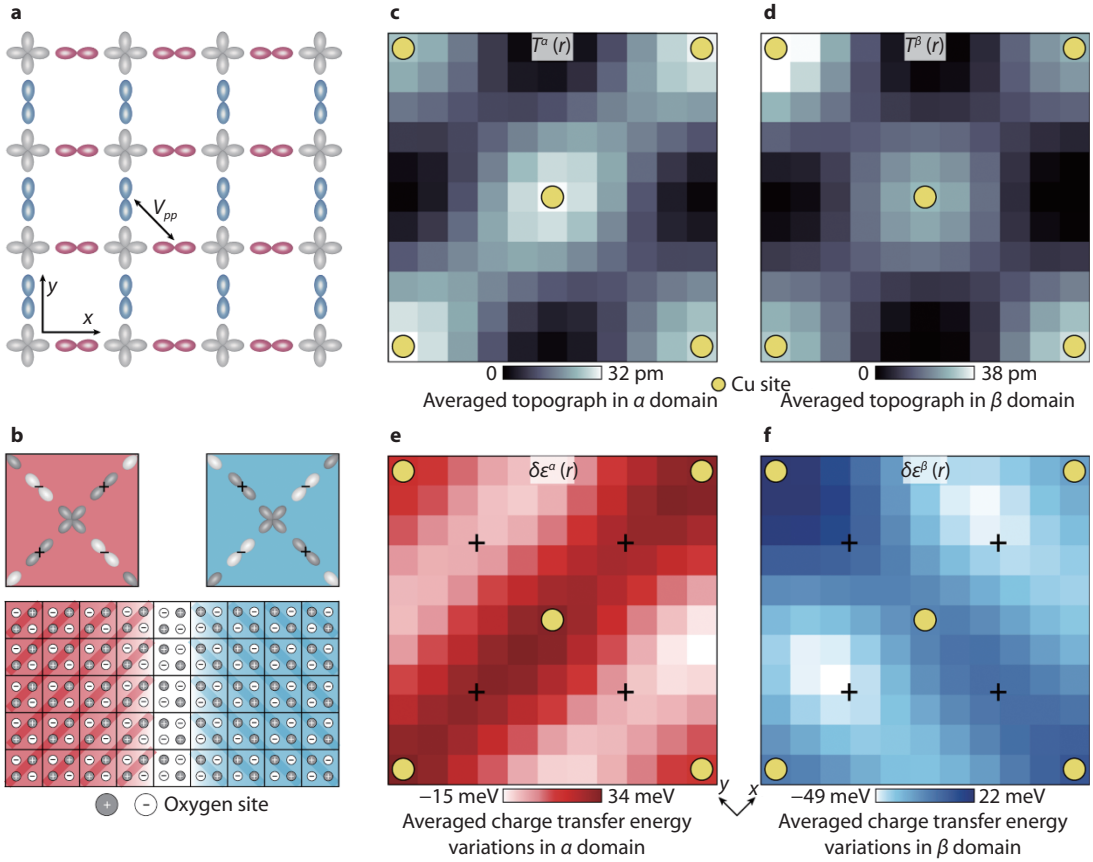


**Fig. 7** Visualization of charge transfer energy and orbital ordering with STM. **a** Schematic of the relevant orbitals in the $CuO_2$ plane depicting the crucial inter-oxygen-orbital Coulomb interaction $V_{pp}$. **b** Schematic of the charge-quadrupole two-level systems within the Ising-domain walls. The top panel shows the schematic of the charge distribution in the four intra-unit-cell oxygen sites consequent to the intra-unit-cell charge transfer symmetry breaking. The bottom panel shows a schematic of two orbitally ordered domains. The darker circles indicate oxygen sites with higher charge transfer energy $\varepsilon$. **c** Unit-cell-averaged structure of $T$(r) averaged over the regions where $N_{\varepsilon} > +5$ meV. **d** Unit-cell-averaged structure of $T$(r) averaged over the regions where $N_{\varepsilon} < -5$ meV. In both c and d, $C_4$ symmetry is preserved. **e** Unit-cell-averaged structure of $\delta\varepsilon$(r) averaged over the regions same as **c**. The charge transfer energy strongly breaks $C_4$ symmetry about every Cu site (yellow dots), and consequently, there is an energy splitting of approximately 50 meV between the charge transfer energies at the two crystal-equivalent oxygen sites (indicated by the crosses). **f** Unit-cell-averaged structure of $\delta\varepsilon$(r) averaged over the regions same as **d**. Virtually identical phenomena as in **e**, but rotated by 90°. The difference between **e** and **f** is the difference in the internal structure of the $CuO_2$ unit cell in the two distinct Ising domains of orbital order[53]. Copyright 2024, Springer Nature.

vised by L. Gu. All authors have approved the final version of the manuscript.

## ■ REFERENCES


1. D. Xiao, L. Gu, *Nano Sel.*, 2020, 1, 183
2. Y. Tokura, M. Kawasaki, N. Nagaosa, *Nat. Phys.*, 2017, 13, 1056
3. Z. Chen, Y. Jiang, Y. T. Shao, M. E. Holtz, M. Odstrcil, M. Guizar-Sicairos, I. Hanke, S. Ganschow, D. G. Schlom, D. A. Muller, *Science*, 2021, 372, 826
4. W. F. Yang, H. Z. Sha, J. Z. Cui, L. Z. Mao, R. Yu, *Nat. Nanotechnol.*, 2024, 19, 612
5. E. Clementi, G. Corongiu, *Int. J. Quantum Chem.*, 2008, 108, 1758
6. J. M. Zuo, M. Kim, M. O'Keeffe, J. C. H. Spence, *Nature*, 1999, 401, 49
7. C. J. Humphreys, *Nature*, 1999, 401, 21
8. J. M. Zuo, M. O'Keeffe, M. Kim, J. C. H. Spence, *Angew. Chem. Int. Ed.*, 2000, 39, 3791
9. W. H. E. Schwarz, *Angew. Chem. Int. Ed.*, 2006, 45, 1508
10. M. Labarca, O. Lombardi, *Found. Chem.*, 2010, 12, 149
11. C. E. Brion, G. Cooper, Y. Zheng, I. V. Litvinyuk, I. E. McCarthy, *Chem. Phys.*, 2001, 270, 13
12. J. Itatani, J. Levesque, D. Zeidler, H. Niikura, H. Pépin, J. C. Kieffer, P. B. Corkum, D. M. Villeneuve, *Nature*, 2004, 432, 867
13. T. Manjo, S. Kitou, N. Katayama, S. Nakamura, T. Katsufuji, Y. Nii, T. -H. Arima, J. Nasu, T. Hasegawa, K. Sugimoto, D. Ishikawa, A. Q. R. Baron, H. Sawa, *Mater. Adv.*, 2022, 3, 3192
14. M. Bugnet, S. Löffler, M. Ederer, D. M. Kepaptsoglou, Q. M. Ramasse, *J. Microsc.*, 2024, 295, 217
15. Y. Tokura, N. Nagaosa, *Science*, 2000, 288, 462
16. J. Zhu, Y. Miao, J. T. Guo, *Acta Mater.*, 1997, 45, 1989
17. J. M. Zuo, *Mater. Trans. Jim*, 1998, 39, 938
18. F. Feng, A. H. Zhang, J. Zhu, *Ultramicroscopy*, 2004, 98, 173
19. J. M. Zuo, *Rep. Prog. Phys.*, 2004, 67, 2053
20. L. J. Wu, Y. M. Zhu, J. Tafto, *Phys. Rev. B*, 1999, 59, 6035
21. Y. M. Zhu, L. J. Wu, J. Tafto, *Microsc. Microanal.*, 2003, 9, 442
22. L. J. Wu, Y. M. Zhu, T. Vogt, H. B. Su, J. W. Davenport, J. Tafto, *Phys. Rev. B*, 2004, 69, 064501
23. K. Tsuda, Y. Ogata, K. Takagi, T. Hashimoto, M. Tanaka, *Acta Cryst. A*, 2002, 58, 514
24. F. Yu, H. M. Zou, J. B. Wang, R. H. Wang, *Micron*, 2004, 35, 411

DOI: 10.54227/mlab.20250002


25. F. Feng, J. Zhu, A. H. Zhang, *Acta Cryst. A*, 2005, 61, 453
26. J. F. Cao, H. M. Zou, C. Guo, Z. L. Chen, S. Z. Pu, *Solid State Ionics*, 2009, 180, 1209
27. P. N. H. Nakashima, A. E. Smith, J. Etheridge, B. C. Muddle, *Science*, 2011, 331, 1583
28. X. Sang, A. Kulovits, G. Wang, J. Wiezorek, *Philos. Mag.*, 2012, 92, 4408
29. D. Peng, P. N. H. Nakashima, *Phys. Rev. Lett.*, 2021, 126, 176402
30. N. K. Hansen, P. Coppens, *Acta Cryst. A*, 1978, 34, 909
31. A. Holladay, P. Leung, P. Coppens, *Acta Cryst. A*, 1983, 39, 377
32. T. Shang, D. Xiao, F. Meng, X. Rong, A. Gao, T. Lin, Z. Tang, X. Liu, X. Li, Q. Zhang, Y. Wen, R. Xiao, X. Wang, D. Su, Y.-S. Hu, H. Li, Q. Yu, Z. Zhang, V. Petricek, L. Wu, L. Gu, J.-M. Zuo, Y. Zhu, C.-W. Nan, J. Zhu, *Nat. Commun.*, 2022, 13, 5810
33. Z. Tang, T. Shang, H. Xu, T. Lin, A. Gao, W. Lin, X. Li, S. Wang, B. Yu, F. Meng, Q. Zhang, X. Wang, D. Su, Q. Meng, L. Wu, L. Gu, C. W. Nan, *Angew. Chem. Int. Ed.*, 2023, 62, e202216898
34. T. Shang, A. Gao, D. Xiao, Q. Zhang, X. Rong, Z. Tang, W. Lin, T. Lin, F. Meng, X. Li, Y. Wen, X. Wang, D. Su, Z. Chen, Y.-S. Hu, H. Li, Q. Yu, Z. Zhang, L. Wu, L. Gu, J.-M. Zuo, Y. Zhu, L. Chen, C.-W. Nan, *Natl. Sci. Rev.*, 2024, 11, nwae255
35. R. F. Egerton, *Ultramicroscopy*, 2012, 119, 24
36. J. C. H. Spence, P. W. Hawkes, *Ultramicroscopy*, 2008, 108, 1502
37. S. Löffler, V. Motsch, P. Schattschneider, *Ultramicroscopy*, 2013, 131, 39
38. L. Pardini, S. Löffler, G. Biddau, R. Hambach, U. Kaiser, C. Draxl, P. Schattschneider, *Phys. Rev. Lett.*, 2016, 117, 036801
39. S. Löffler, M. Bugnet, N. Gauquelin, S. Lazar, E. Assmann, K. Held, G. A. Botton, P. Schattschneider, *Ultramicroscopy*, 2017, 177, 26
40. J. Fink, *Adv. Electron. Electron Phys.*, 1989, 75, 121
41. J. Fink, N. Nucker, E. Pellegrin, H. Romberg, M. Alexander, M. Knupfer, *J. Electron. Spectrosc.*, 1994, 66, 395
42. A. Torres-Pardo, A. Gloter, P. Zubko, N. Jecklin, C. Lichtensteiger, C. Colliex, J. M. Triscone, O. Stéphan, *Phys. Rev. B*, 2011, 84, 220102
43. K. Xu, L. Zhang, A. Godfrey, D. Song, W. Si, Y. Zhao, Y. Liu, Y. Rao, H. Zhang, H. A. Zhou, W. Jiang, W. Wang, Z. Cheng, J. Zhu, *Proc. Natl. Acad. Sci. U.S.A.*, 2021, 118, e2101106118
44. C. Iwashimizu, M. Haruta, H. Kurata, *Appl. Phys. Lett.*, 2021, 119, 232902
45. M. Bugnet, M. Ederer, V. K. Lazarov, L. Li, Q. M. Ramasse, S. Löffler, D. M. Kepaptsoglou, *Phys. Rev. Lett.*, 2022, 128, 116401
46. M. Ederer, S. Löffler, *Ultramicroscopy*, 2024, 256, 113866
47. A. J. D'Alfonso, B. Freitag, D. Klenov, L. J. Allen, *Phys. Rev. B*, 2010, 81, 100101
48. J. S. Jeong, M. L. Odlyzko, P. Xu, B. Jalan, K. A. Mkhoyan, *Phys. Rev. B*, 2016, 93, 165140
49. H. J. Lee, W. Ho, *Science*, 1999, 286, 1719
50. J. Repp, G. Meyer, S. Paavilainen, F. E. Olsson, M. Persson, *Science*, 2006, 312, 1196
51. L. Gross, N. Moll, F. Mohn, A. Curioni, G. Meyer, F. Hanke, M. Persson, *Phys. Rev. Lett.*, 2011, 107, 086101
52. H. Kim, Y. Yoshida, C. C. Lee, T. R. Chang, H. T. Jeng, H. Lin, Y. Haga, Z. Fisk, Y. Hasegawa, *Sci. Adv.*, 2017, 3, eaao0362
53. S. Wang, N. Kennedy, K. Fujita, S.-I. Uchida, H. Eisaki, P. D. Johnson, J. C. S. Davis, S. M. O'Mahony, *Nat. Mater.*, 2024, 23, 492
54. H. Hafiz, K. Suzuki, B. Barbiellini, Y. Orikasa, V. Callewaert, S. Kaprzyk, M. Itou, K. Yamamoto, R. Yamada, Y. Uchimoto, Y. Sakurai, H. Sakurai, A. Bansil, *Sci. Adv.*, 2017, 3, e1700971
55. H. Yavaş, M. Sundermann, K. Chen, A. Amorese, A. Severing, H. Gretarsson, M. W. Haverkort, L. H. Tjeng, *Nat. Phys.*, 2019, 15, 559
56. S. Kitou, T. Manjo, N. Katayama, T. Shishidou, T.-H. Arima, Y. Taguchi, Y. Tokura, T. Nakamura, T. Yokoyama, K. Sugimoto, H. Sawa, *Phys. Rev. Res.*, 2020, 2, 033503
57. S. Kitou, Y. Kaneko, Y. Nakamura, K. Sugimoto, Y. Nomura, R. Arita, Y. Tokura, H. Sawa, T. H. Arima, *Phys. Rev. B*, 2023, 108, 024103
58. P. Coppens, B. Iversen, F. K. Larsen, *Coordin. Chem. Rev.*, 2005, 249, 179
59. R. Kaminski, S. Domagala, K. N. Jarzembska, A. A. Hoser, W. F. Sanjuan-Szklarz, M. J. Gutmann, A. Makal, M. Malinska, J. M. Bak, K. Wozniak, *Acta Cryst. A*, 2014, 70, 72
60. H. Kasai, K. Tolborg, M. Sist, J. Zhang, V. R. Hathwar, M. Ø. Filsø, S. Cenedese, K. Sugimoto, J. Overgaard, E. Nishibori, B. B. Iversen, *Nat. Mater.*, 2018, 17, 249
61. C. Gao, A. Genoni, S. Gao, S. Jiang, A. Soncini, J. Overgaard, *Nat. Chem.*, 2020, 12, 213
62. C. Ophus, *Microsc. Microanal.*, 2019, 25, 563
63. K. M. Müller-Caspary, M. Duchamp, M. Rösner, V. Migunov, F. Winkler, H. Yang, M. Huth, R. Ritz, M. Simson, S. Ihle, H. Soltau, T. Wehling, R. E. D. Dunin-Borkowski, S. Van Aert, A. Rosenauer, *Phys. Rev. B*, 2018, 98, 121408
64. S. Fang, Y. Wen, C. S. Allen, C. Ophus, G. G. D. Han, A. I. Kirkland, E. Kaxiras, J. H. Warner, *Nat. Commun.*, 2019, 10, 1127
65. W. P. Gao, C. Addiego, H. Wang, X. X. Yan, Y. S. Hou, D. X. Ji, C. Heikes, Y. Zhang, L. Z. Li, H. X. Huyan, T. Blum, T. Aoki, Y. F. Nie, D. G. Schlom, R. Q. Wu, X. Q. Pan, *Nature*, 2019, 575, 480
66. J. Martis, S. Susarla, A. Rayabharam, C. Su, T. Paule, P. Pelz, C. Huff, X. T. Xu, H. K. Li, M. Jaikissoon, V. Chen, E. Pop, K. Saraswat, A. Zettl, N. R. Aluru, R. Ramesh, P. Ercius, A. Majumdar, *Nat. Commun.*, 2023, 14, 4363
67. L. Susana, A. Gloter, M. Tencé, A. Zobelli, *ACS Nano*, 2024, 18, 7424
68. S. Löffler, M. Ederer, *Microsc. Microanal.*, 2023, 29, 376
69. L. J. Wu, Q. P. Meng, Y. M. Zhu, *Ultramicroscopy*, 2020, 219, 113095
70. T. Friedrich, C.-P. Yu, J. Verbeeck, S. Van Aert, *Microsc. Microanal.*, 2023, 29, 395
71. B. Diederichs, Z. Herdegen, A. Strauch, F. Filbir, K. Müller-Caspary, *Nat. Commun.*, 2024, 15, 101